Bioinspiration & Biomimetics

PAPER

Slithering towards autonomy: a self-contained soft robotic snake platform with integrated curvature sensing

Ming Luo, Yixiao Pan, Erik H Skorina, Weijia Tao, Fuchen Chen, Selim Ozel and Cagdas D Onal

Soft Robotics Laboratory, Worcester Polytechnic Institute, Worcester, MA, USA

**E-mail:** cdonal@wpi.edu

Abstract

Soft robotic snakes promise significant advantages in achieving traveling curvature waves with a reduced number of active segments as well as allowing for safe and adaptive interaction with the environment and human users. However, current soft robot platforms suffer from a lack of accurate theoretical dynamic models and proprioceptive measurements, which impede advancements toward full autonomy. To address this gap, this paper details our recent results on the design, fabrication, and experimental evaluation of a new-generation pressure-operated soft robotic snake platform we call the WPI SRS, which employs custom magnetic sensors embedded in a flexible backbone to continuously monitor the curvature of each of its four bidirectional bending segments. In addition, we present a complete and accurate dynamic undulatory locomotion model that accounts for the propagation of frictional moments to describe linear and rotational motions of the SRS. Experimental studies indicate that on-board sensory measurements provide accurate real-time curvature feedback, and numerical simulations offer a level of abstraction for lateral undulation under ideal conditions.

1. Introduction

Pneumatically operated soft robots made of silicone rubber [1–7] offer many advantages over rigid robots. Due to the properties of this soft material, a soft robot has increased levels of mechanical flexibility and can operate more safely in environments with humans than robots with traditional links. In addition, such a soft robot [8–11] could be cheap and easily manufactured, with the bulk of the fabrication process being the molding of silicone. However, compared with the traditional rigid systems from an engineering perspective, there are several unsolved problems in the development of an autonomous soft robot. Precise control of a continuously deformable body is challenging, since it has infinite passive degrees of freedom. Experiences on rigid robots suggest that the potential solution should include an accurate but straightforward model that describes the robot's dynamic behavior and a sensor to report the state of the robot for use in closed-loop control. For true mobility, fluidic soft robots [12, 13] should carry their pressure sources on board. Our prior work provided three approaches to realize power autonomy for soft robots [14–18], while other recent work in the literature focused on untethered self-contained operation [19, 20]. A comparative review of potential energy sources is provided in [21]. However, power autonomy is only the first step towards full autonomy, and none of these soft robots in the literature possess proprioceptive sensors to provide state feedback.

We previously presented a novel pressure-operated soft robotic snake [16, 22, 23]. The body of this soft robotic snake prototype is comprised of four bidirectional fluidic elastomer actuators composed in series as actuator segments pressurized by controlling the binary state of a solenoid valve array. Compared with traditional rigid snake robots [24–28], our soft robotic snake is inherently safer and adaptable under unpredictable environments, allowing physical contact, which promises to reduce the burden on planning and control algorithms. In order to improve the dynamic features of our soft snake robot, we recently introduced new soft actuation segments [29] and a new-generation four-segment snake, utilizing these bending actuators [30], which can locomote using

Figure 1. CAD model (left) and experimental prototype (right) of the self-contained soft robotic snake.
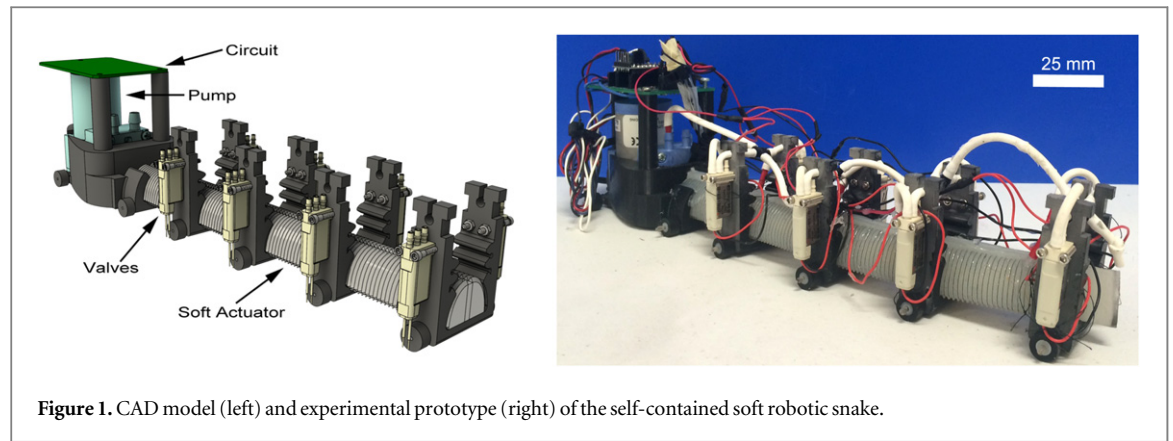
lateral undulation 10 times faster than the original prototype when pressurized air is supplied using external tubing.

To understand the dynamics of soft undulatory locomotion, our previous work also presented a theoretical dynamic model of a soft snake robot made of constant-curvature bending segments and experimentally verified its accuracy and predictive power over linear locomotion trajectories (pure translation) [22]. Other works on modeling soft continuous structures focus on kinematics, not dynamics [31, 32]. This approach treats each soft segment as an actuated bending joint and solid connectors between segments as links, combining a kinematic model based on segment curvatures, inspired by rigid snake modeling efforts [33–38], with a dynamic model for pressure-driven soft actuators [16, 29].

Towards the ultimate goal of full autonomy, this paper introduces a fully self-contained soft robotic snake (WPI SRS) as a mobility platform, which incorporates on-board electrical and fluidic power, embedded control, and distributed solenoid valves for tetherless operation (figure 1). Custom magnetic curvature sensors are incorporated within each soft bending actuation segment for real-time proprioceptive measurements. Finally, a complete dynamic soft undulation model [30] is proposed to predict steering motions through a careful analysis of rotational dynamics due to moments induced by anisotropic friction forces.

The self-contained soft robotic snake platform developed in this paper is inspired by the traveling curvature waveform observed in biological snakes. Unlike rigid snake robots, our system has a continuously deformable slender body to generate smooth curvature waves. The deformability of the silicone rubber body and the dynamic behavior of the soft actuators make this robot a good candidate for accurately reproducing the snake locomotion observed in nature. Curvature proprioception has other bioinspired parallels and functional utility. When a biological snake traverses terrain with irregularities, it adjusts its torques based on its body shape [39], which creates lateral holds to push the body forward. This behavior results in obstacle-aided locomotion, where obstacles may be created by the body as sand lines. For traditional rigid

snake robots, it is difficult to realize this, because the rigid snake robot shape is not continuous, and it is difficult to modulate contact forces from the obstacle. A snake robot with series elastic actuator joints is still insufficient for replicating the obstacle-aided locomotion observed in biological snakes [40]. These findings from the biological snake inspire our efforts to incorporate proprioceptive curvature sensing in our system towards a torque-controlled locomotion approach.

The contributions of this paper include:

- Development and experimental evaluation of the first soft robotic snake with accurate proprioceptive curvature sensing.

- Multi-layer composite fabrication process for soft robotic structures with integrated flexible electronics.

- A complete dynamic soft snake model which can predict the rotational motion of the robot on curved trajectories.

The rest of this paper is organized as follows: section 2 describes our soft snake dynamic model and the fabrication processes of the elastomeric body and the curvature sensors, as well as the system architecture of the SRS. Section 3 details our results on verification of the presented dynamic model for a range of operational parameters and the performance of the curvature sensors through experimental studies. Section 4 discusses our subsequent conclusions and plans to continue this work in the future.

2. Methods

2.1. Locomotion dynamics of a segmented soft robotic snake

The complete dynamic model is fundamentally based on the balance of forces and torques for each end of each segment (figure 2). Table 1 lists all the kinematic and dynamic parameters of the SRS model. Compared with our previous model [22], the refined model incorporates the moments generated by the anisotropic
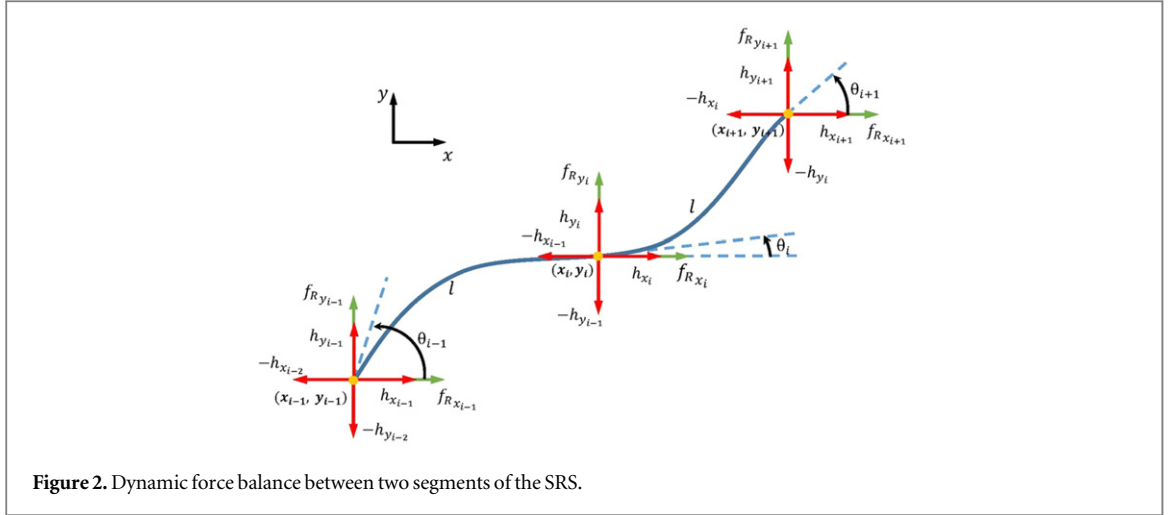
Figure 2. Dynamic force balance between two segments of the SRS.

Table 1. Parameters of the SRS dynamic model.

Symbol	Description
N	Number of links
l	The channel length of the soft segment
m	Mass of each link
J	Moment of inertia of each link
μ_t	Tangential coefficient of friction of each link
μ_n	Normal coefficient of friction of each link
$\boldsymbol{\theta} \in \mathbb{R}^N$	Link global orientation vector
$\boldsymbol{\kappa} \in \mathbb{R}^{N-1}$	Segment curvature vector
$X, Y \in \mathbb{R}^N$	Link CoM global coordinates vectors
(p_x, p_y)	Global coordinates of the CoM of the robot
$T \in \mathbb{R}^{N-1}$	Segment torque input vector
$f_{R,x}, f_{R,y} \in \mathbb{R}^N$	Ground friction force vectors
$h_x, h_y \in \mathbb{R}^{N-1}$	Joint constraint force vectors

friction forces acting on the soft segments, which are graphically depicted in figure 3. From this, the force balance equation can be written as:

$$m\ddot{X} = f_R, x + D^T h_x,$$
$$m\ddot{Y} = f_R, y + D^T h_y, \tag{1}$$

where $D = \begin{pmatrix} 1 & -1 & & 0 \\ & \cdot & \vdots & \cdot \\ 0 & & 1 & -1 \end{pmatrix} \in \mathbb{R}^{(N-1)\times N}$.

Figure 3 displays the torque balance for each soft segment. F_{Li} and F_{Ri} represent the external forces perpendicular to the moment arm for points A and B on segment i, which include the joint constraint force and friction. Joint constraint forces ensure that two segments remain connected, and frictional forces are anisotropic between the tangential and normal directions [16]. In order to calculate these moment-generating forces, the sum of the joint constraint force and friction in figure 2 should be projected to the moment-arm normal direction. The projection angles $\theta_{F_{Li}}$, $\theta_{F_{Ri}}$, respectively, for A and B can be calculated by:

For point A: $\theta_{F_{Li}} = \frac{\pi}{2} + \frac{\theta_{i-1}}{2} + \frac{\theta_i}{2}$

For point B: $\theta_{F_{Ri}} = \frac{3\pi}{2} + \frac{\theta_i}{2} + \frac{\theta_{i+1}}{2}$

Let $h_{x,i}^\star$, $f_{Rx,i}^\star$ be the constraint and friction forces in line with the moment-generating force on segment i, written as:

$$h_{x,i}^\star = h_{x,i} \cos\left(\theta_{R_i}\right) + h_{y,i} \sin\left(\theta_{R_i}\right)$$
$$f_{Rx,i}^\star = f_{Rx,i} \cos\left(\theta_{R_i}\right) + f_{Ry,i} \sin\left(\theta_{R_i}\right) \tag{2}$$

The length of the moment arm changes as the segment curvature changes. According to the geometric relation shown in figure 3, the length of the moment arm is given by:

$$l_i = 2 \left| \frac{l}{\Delta\theta} \sin \frac{\Delta\theta}{2} \right| \tag{3}$$

The approximated inertia of each soft-actuator end point is given by:

$$j(i) = \begin{cases} ml_1^2/3 & \text{if } i = 1 \\ ml_{N-1}^2/3 & \text{if } i = N \\ ml_{i-1}^2/3 + ml_i^2/3 & \text{otherwise} \end{cases}$$

The inertia matrix of the entire soft snake is, then:

$$J = \begin{pmatrix} j(1) & 0 & & \\ 0 & j(2) & & \\ & & \cdot\ \cdot & 0 \\ & & 0 & j(N) \end{pmatrix} \in \mathbb{R}^{N\times N} \tag{4}$$

Therefore, the torque balance equation for segment i is:

$$j(i)\ddot{\theta}_i = T_i - T_{i-1} + l_{i-1}\left(h_{x,i-1}^\star - h_{x,i-2}^\star\right)$$
$$+ l_i\left(h_{x,i+1}^\star - h_{x,i}^\star\right) + l_{i-1}f_{Rx,i-1}^\star + l_i f_{Rx,i+1}^\star, \tag{5}$$

where T_i is the torque with respect to the ith point generated by the input pressure and material deformation. Defining $t_i = \frac{\theta_{i-1}}{2} + \frac{\theta_i}{2}$, we can plug equations (3) and (4) into (5) to reveal the torque balance for the entire snake:

$$J\ddot{\boldsymbol{\theta}} = D^T T - H_1 C_1 h_x + H_2 C_1 h_x + H_3 C_2 h_y$$
$$- H_4 C_2 h_y - H_5 f_{R,x} + H_7 f_{R,x} + H_6 f_{R,y}$$
$$- H_8 f_{R,y} \tag{6}$$

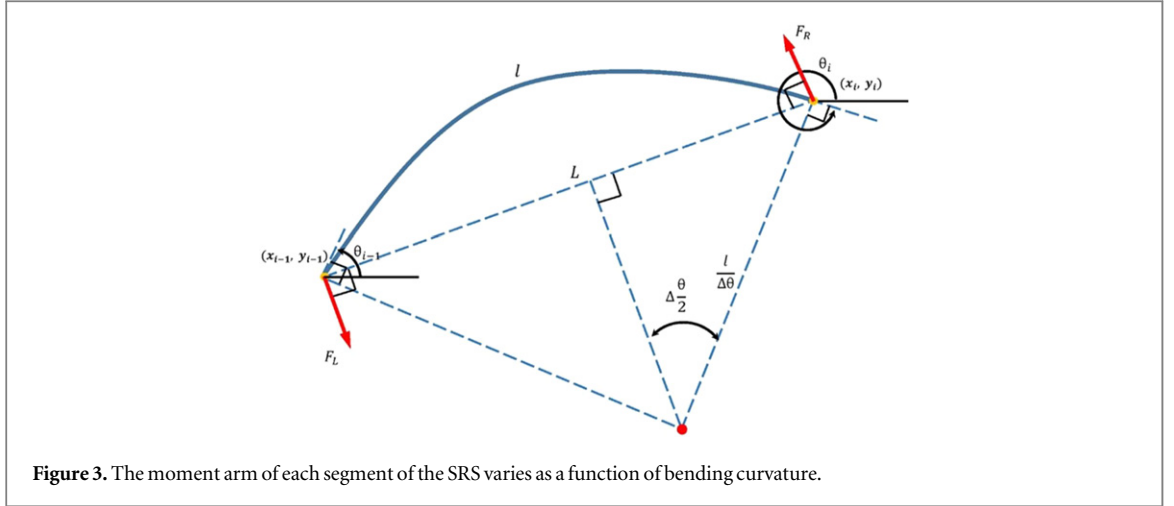**Figure 3.** The moment arm of each segment of the SRS varies as a function of bending curvature.

$H_1 = A_1$ where $C_{i,i} = l_{i-1} \sin t_{i-1}$

$H_2 = A_1$ where $C_{i,i} = l_{i-1} \cos t_{i-1}$

$H_3 = A_2$ where $C_{i,i} = l_i \sin t_i$

$H_4 = A_2$ where $C_{i,i} = l_i \cos t_i$

$H_5 = A_3$ where $C_{i,i-1} = l_{i-1} \sin t_{i-1}$

$H_6 = A_4$ where $C_{i,i-1} = l_{i-1} \cos t_{i-1}$

$H_7 = A_3$ where $C_{i,i+1} = l_i \sin t_i$

$H_8 = A_4$ where $C_{i,i+1} = l_i \cos t_i$

Equations (7) describe below the format of the matrices H_1–H_8 for the given C elements for each case:

$$A_1 = \begin{pmatrix} 0 & 0 & & \\ 0 & C_{2,2} & & \\ & & \ddots & \ddots \\ & & 0 & C_{N-1,N-1} \\ & & & 0 & C_{N,N} \end{pmatrix},$$

$$A_2 = \begin{pmatrix} C_{1,1} & 0 & & \\ 0 & C_{2,2} & & \\ & & \ddots & \ddots \\ & & C_{N-1,N-1} & 0 \\ & & & 0 & 0 \end{pmatrix} \in \mathbb{R}^{N \times N}$$

$$A_3 = \begin{pmatrix} 0 & 0 & & \\ C_{2,1} & 0 & & \\ & & \ddots & \ddots \\ & & 0 & 0 \\ & & C_{N,N-1} & 0 \end{pmatrix},$$

$$A_4 = \begin{pmatrix} 0 & C_{1,1} & & \\ 0 & 0 & & \\ & & \ddots & \ddots \\ & & 0 & C_{N-1,N-1} \\ & & & 0 & 0 \end{pmatrix} \in \mathbb{R}^{N \times N}$$

$$C_1 = \begin{pmatrix} 0 & 0 & & \\ 1 & 0 & & \\ & & \ddots & \ddots \\ & & 1 & 0 \\ & & -1 & 1 \end{pmatrix},$$

$$C_2 = \begin{pmatrix} -1 & 1 & & \\ 0 & -1 & & \\ & & \ddots & \ddots \\ & & 0 & -1 \\ & & 0 & 0 \end{pmatrix} \in \mathbb{R}^{N \times (N-1)} \quad (7)$$

We can combine equations (1) and (6) to yield:

$$M_\theta \ddot{\theta} + W_\theta \dot{\theta}^2 + G_\theta \dot{\theta} + M_\kappa \ddot{\kappa} + W_\kappa \dot{\kappa}^2$$
$$+ F_1 f_{R,x} + F2 f_{R,y} = D^{TT} Nm \begin{bmatrix} \ddot{X} \ddot{Y} \end{bmatrix}^T = E^T f_R \quad (8)$$

$$M_\theta = J I_N + ml H_9 \left(\Gamma \Gamma^T \right)^{-1} B_1 + ml H_{10} \left(\Gamma \Gamma^T \right)^{-1} B$$

$$W_\theta = ml H_9 \left(\Gamma \Gamma^T \right)^{-1} B_3 - ml H_{10} \left(\Gamma \Gamma^T \right)^{-1} B_1$$

$$G_\theta = ml H_9 \left(\Gamma \Gamma^T \right)^{-1} B_4 + ml H_{10} \left(D D^T \right)^{-1} B_7$$

$$M_\kappa = ml H_9 \left(\Gamma \Gamma^T \right)^{-1} B_5 + ml H_{10} \left(\Gamma \Gamma^T \right)^{-1} B_8$$

$$W_\kappa = ml H_9 \left(\Gamma \Gamma^T \right)^{-1} B_6 + ml H_{10} \left(\Gamma \Gamma^T \right)^{-1} B_9$$

$$F_1 = H_{11} \left(\Gamma \Gamma^T \right)^{-1} D - H_{13}$$

$$F_2 = -H_{12} \left(\Gamma \Gamma^T \right)^{-1} D + H_{14}$$

$$E = \begin{pmatrix} e & 0_{N \times 1} \\ 0_{N \times 1} & e \end{pmatrix} \in \mathbb{R}^{2N \times 2}$$

$$e = \begin{pmatrix} 1 & , & \ldots & , & 1 \end{pmatrix}^T \in \mathbb{R}^N$$

$$(9)$$

$H_9 = (H_3 C_2 - H_1 C_1)$, $H_{10} = (H_4 C_2 - H_2 C_1)$, $H_{11} = (H_3 - H_1)$, $H_{12} = (H_4 - H_2)$, $H_{13} = (H_7 - H_5)$, $H_{14} = (H_8 - H_6)$.

This set of equations provides an accurate mathematical representation of the ideal dynamics of our soft snake robot.

2.2. Custom magnetic curvature sensors

We recently proposed an approach to measuring curvatures using a magnet and a Hall element on a flexible circuit [41], where we focused on the development and characterization of this new technique. In contrast, in this paper we focus on the system-level integration of these sensors, embedding them within the silicone rubber body in the backbone of the SRS using a composite molding process. Compared to commercial resistive curvature sensors, this sensor offers a fast dynamic response, no nonlinear artifacts,
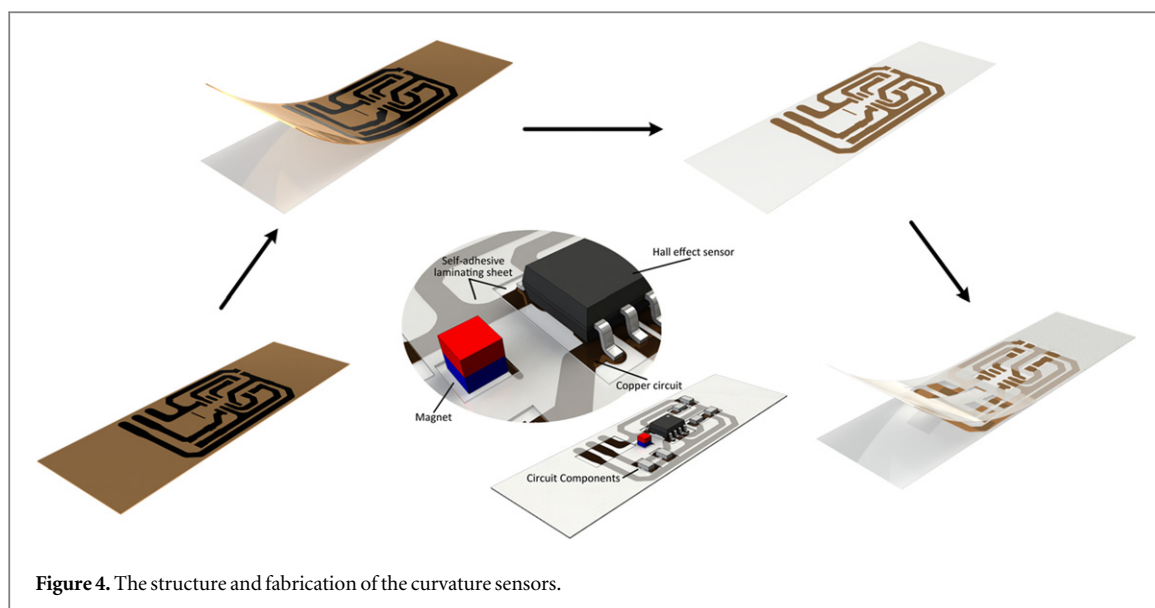
Figure 4. The structure and fabrication of the curvature sensors.

and the ability to customize sensitivity and range in order to measure curvature values according to a variety of task specifications. Compared to optical fiber curvature sensors [31], our sensor is easier to fabricate and is more scalable.

In the center of our robot is an inextensible layer that prevents the segments from extending, constraining the actuator deformation to pure bending. This inextensible layer becomes the neutral axis of bending, subject to no length change and minimal bending stresses. Therefore, this thin center constraint is the optimal location to embed flexible curvature sensors.

Since the middle constraint layer needs to be as thin as possible, a miniature NeFeB magnet is utilized (a 1.5875 mm cube), and sensitivity is adjusted to measure curvatures up to $0.35\,cm^{-1}$ based on initial motion-capture experiments. To minimize the influence of the sensor on the dynamic behavior of soft bending segments, we use a thin plastic circuit substrate by using a polyester lamination film. Finally, we used a laser-machined layer of lamination film on the top surface to keep copper traces tightly bonded to the substrate.

The entire fabrication process consists of five steps, as explained below and illustrated in figure 4:

Step 1: Circuit traces are designed and printed on a copper film using a solid-ink printer.

Step 2: The patterned copper film is laminated with a thin polyester lamination film on the back side.

Step 3: The copper-polyester laminate is placed in a ferric chloride etching tank, to remove all exposed copper, leaving the electrical traces intact.

Step 4: Another layer of laminating sheet is laser-machined to leave mounting and connection holes for discrete components and laminated to the top side of the flexible circuit.

Step 5: Discrete circuit components are soldered, and the miniature magnet is mounted on its precise position under a microscope.

2.3. Fabrication process of the SRS body

The entire fabrication process of the SRS, which uses four bidirectional bending actuators as segments, consists of four steps, as explained below and illustrated in figure 5:

Step 1: Body mold and constraint mold are 3D printed. The body mold has two parts: the holder, which has the main shape of the actuator, and the cover, which helps form the shape of the channel. The constraint mold is a rectangular shell.

Step 2: Ecoflex 00–30 silicone rubber is mixed and introduced into all molds. After the silicone fills the body mold, the cover is placed on top to create the fluidic chamber. Four curvature sensors are inserted into the constraint mold. Two half-bodies are molded at the same time.

Step 3: Thread is tied, following the grooves around the body. Uncured silicone rubber is brushed to cover the thread to make sure it stays in place and attached to the main body.

Step 4: Finally, the two half-bodies and constraint layer are bonded to each other using a very thin layer of uncured silicone rubber.

2.4. System architecture and control

Figure 6 shows the system architecture of the SRS. 3A-D printed valve and passive wheel holders (links) are placed around the SRS body between each bending module. Passive wheels provide the requisite

Figure 5. Fabrication process of the soft robotic snake.
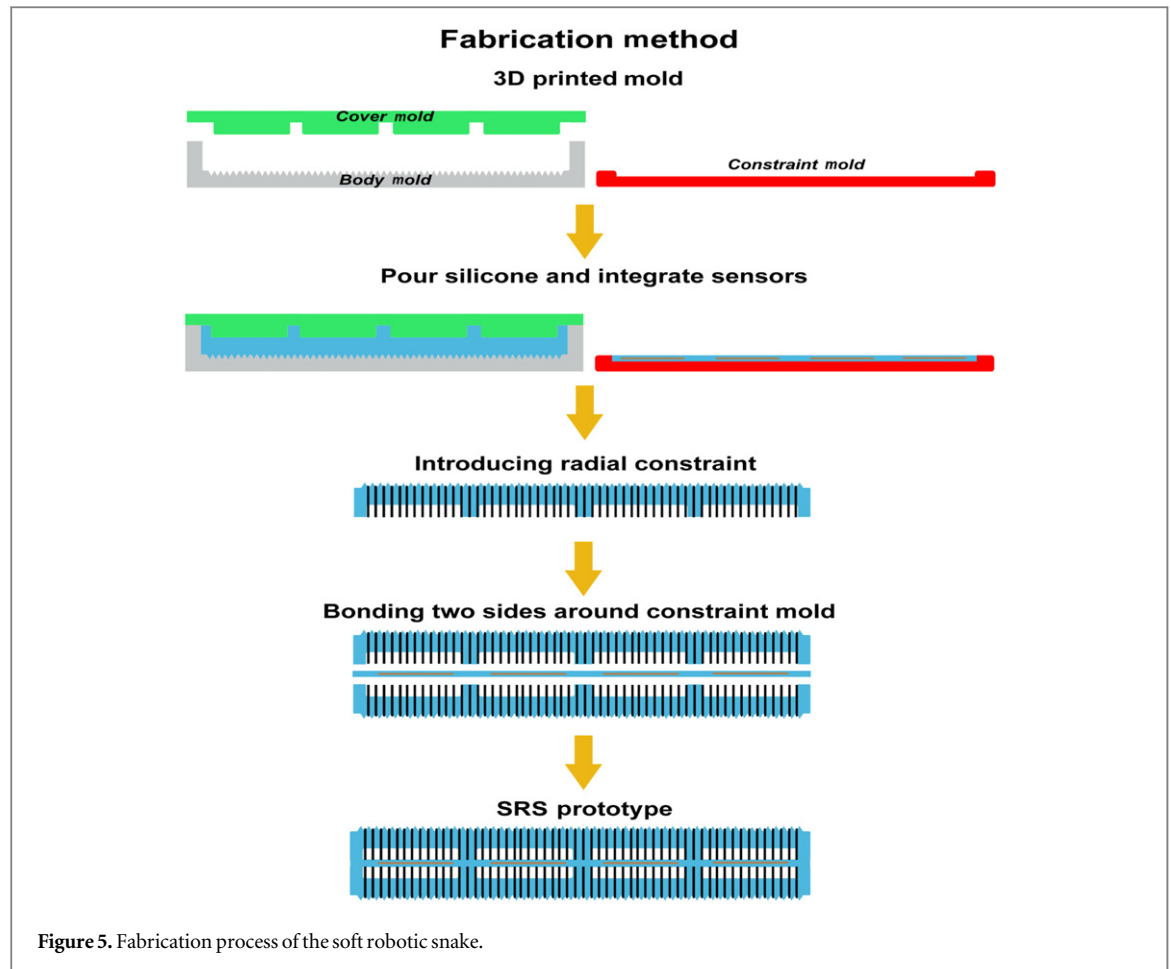
anisotropic friction between tangential and normal directions of the body. Each miniature solenoid valve, controlled by the Arduino Mini Pro Board, directs pressurized air into a single soft actuator. The pressure source is a Parker C134G-13 compressor embedded at a 3-D printed tail, which delivers up to 16 psi at 2 LPM. To keep the actuators operating within a safe range, the microcontroller sends a pulse width modulation (PWM) signal to the common collector of the compressor to adjust its output pressure. All experimental results that follow utilize a PWM duty cycle of 90%. Analog input pins of the microcontroller read the sensor data from the embedded curvature sensors. The SRS can communicate with a nearby PC via Xbee wireless communication, which is used to record curvature data and reprogram the microcontroller. In order to verify the performance of the curvature sensor as well as the whole snake, a custom overhead motion capture system using an Optitrack V120-SLIM camera and a large-power infrared (IR) light-emitting diode array are used as a ground truth external measurement system that tracks passive 3 mm IR markers. Two markers are placed at each valve holder and the tail such that the position and angle of each link as well as the bending angle of each actuator can be measured.

The binary operational state of the miniature solenoid valves is determined by the following traveling wave, based on the serpenoid equation [24]:

$$S_i = sign\left(\sin\left(\omega t + \beta_i\right) + \phi\right), \qquad (10)$$

where ω, β_i, and ϕ, are the frequency, traveling wave delay, and offset of the ith actuator, respectively. The solenoid valve is open when $S_i > 0$ and is closed otherwise.

3. Results and discussion

Simulations treat the last link and the tail as a single-point mass. Therefore, the tail mass is different from the other four links. Table 2 displays the experimental parameter values, where m_T is the mass of the tail.

During experimental studies, the soft snake was operated at frequencies from 0.75–1 Hz with the offset ranging from −0.2–0.2. Figure 7 shows the position of the soft snake at increments of 6 s when the frequency is 1 Hz and the offset the is 0.2. The input pressure was fixed throughout all of the experiments at a value that was too high for the actuators to withstand at steady state. To minimize the time each actuator was pressurized, we constrained the frequencies to remain above 0.75 Hz and the absolute value of the offset to be below 0.2.

Figure 8 shows a series of SRS states over a 10 s time interval, comparing simulated results against the
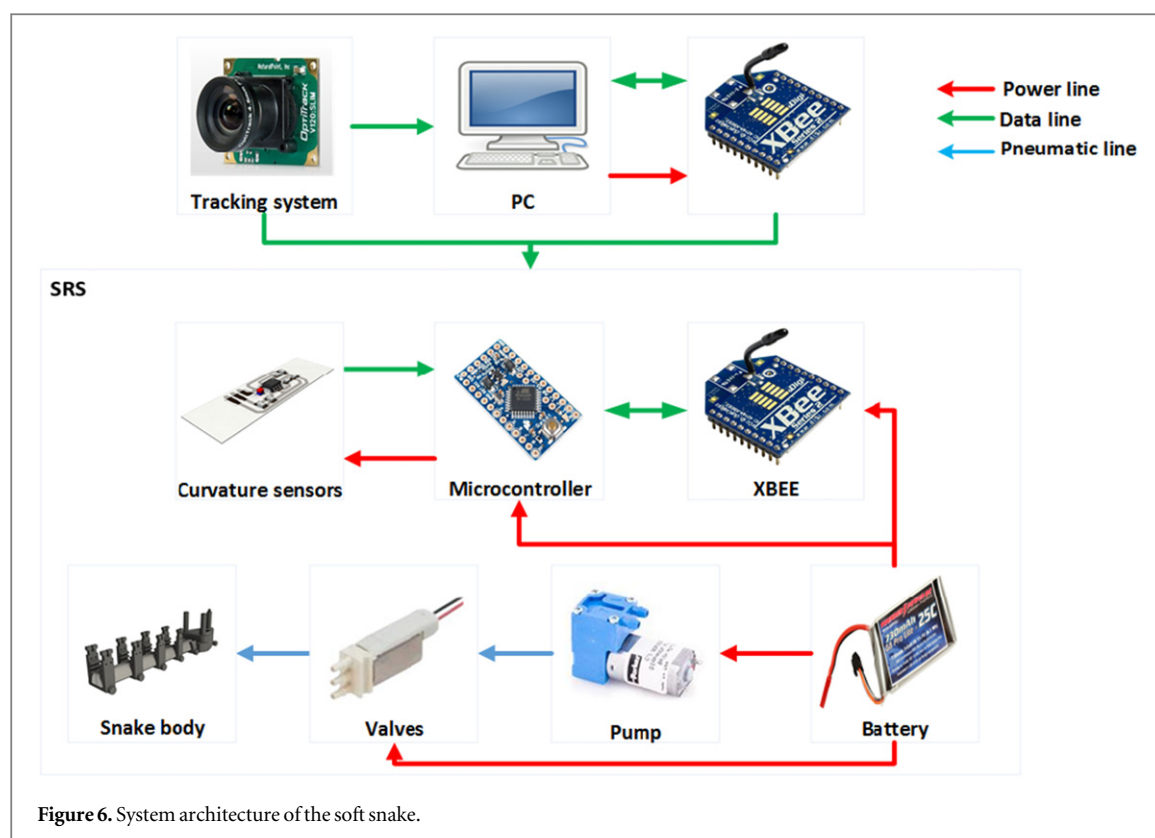
Figure 6. System architecture of the soft snake.

Table 2. Experimental parameters.

N	l	m	m_T	μ_t	μ_n	β_i
5	37 mm	52.5 g	267.6 g	0.043	0.57	$\frac{2\pi i}{N-1}$

experimental results. At each state, the circle represents the snake's head, and the curve is the rest of the snake trailing behind. In the experimental plot, some snake states have much larger curvatures then the others. This is a result of errors in the motion-capture data, as the curvature sensors do not provide global position information. In the simulation, the zero-offset path of the snake was directly along the vertical axis, with offset paths curving symmetrically to the right and to the left. The experimental snake exhibits a bias to the left, which can be corrected by giving a negative offset. This is likely the result of inconsistencies in the fabrication process, which create different bending properties on either side. In addition, due to curvature sensor requirements (circuit components are placed on one side of the plastic substrate), the constraint layer (the neutral axis) is slightly off-center, biasing a single direction of steering. It should be noted that, given the minimum allowable offset of -0.2 in these experiments, the current snake can only turn right over exceedingly large radii. Using larger negative offset values may enable steering in both directions for smaller pressure input values. The fabrication process may be revised to position the constraint layer at a different location that yields the same amount of bending in both directions.

Figure 9 shows a comparison of the linear velocities of the center of mass (CoM) of the SRS between simulation and experimental results. From the plots, it can be seen that the general behavior of the experimental snake is captured by the model. The differences between the model predictions and experimental results are likely the result of measurement errors, fabrication inconsistencies, and varying friction coefficients on different areas of surface. Figure 10 shows the CoM angular velocities for the simulated model predictions and experimental results under offset values of 0.1 and 0.2. The CoM angular velocities were too small for offsets of 0, -0.1, -0.2 to give meaningful data. As with the linear velocity, the model also predicts physical snake behavior with relative accuracy, especially considering the inconsistencies in the SRS prototype. However, the simulation results display a slight trend of reducing angular velocities with increasing frequency. This makes sense, as an increase in frequency reduces the amplitude of the curvature waveform, which translates as slightly reduced linear velocity. A corresponding effect on the angular velocity is visible, which is calculated as the linear velocity of the CoM around a radius of curvature. Angular velocity measurements are subject to a lot of experimental variation, since linear velocities and radius-of-curvature values both include uncertainty, leading to larger variations in angular velocity measurements. However, the numerical predictions stay within these experimental variations, where trends are difficult to capture.
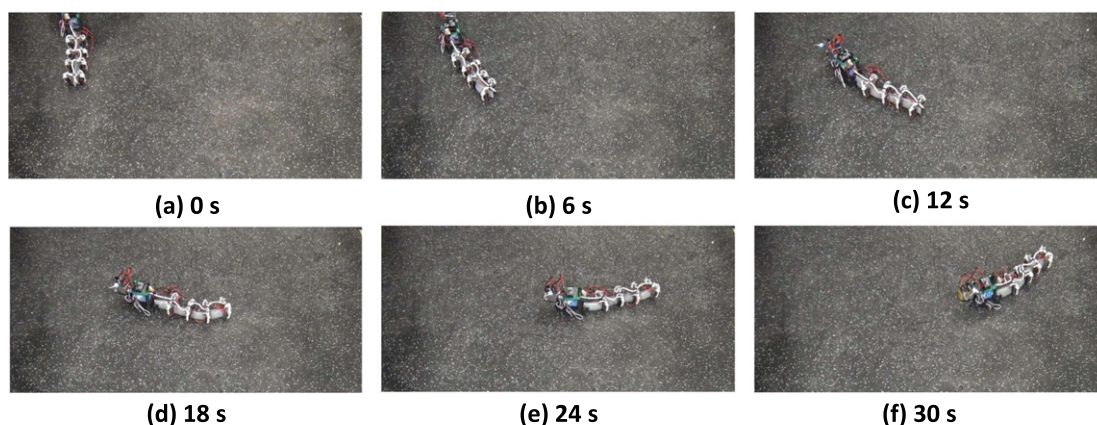
Figure 7. A series of still images, each 6 s apart, taken to show the snake in operation. The frequency is 1 Hz, and the offset is 0.2.

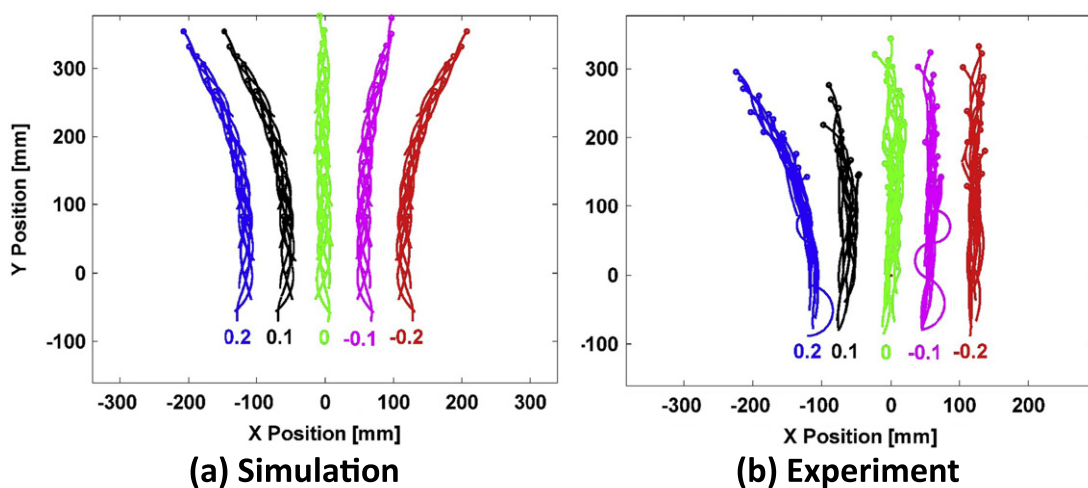

(a) Simulation

(b) Experiment

Figure 8. SRS shape and trajectory when the frequency is 0.9 Hz and the offset is 0.2 (blue), 0.1 (black), 0 (green), −0.1 (pink), and −0.2 (red) in the simulation (**a**) and experiment (**b**) in 10 s.
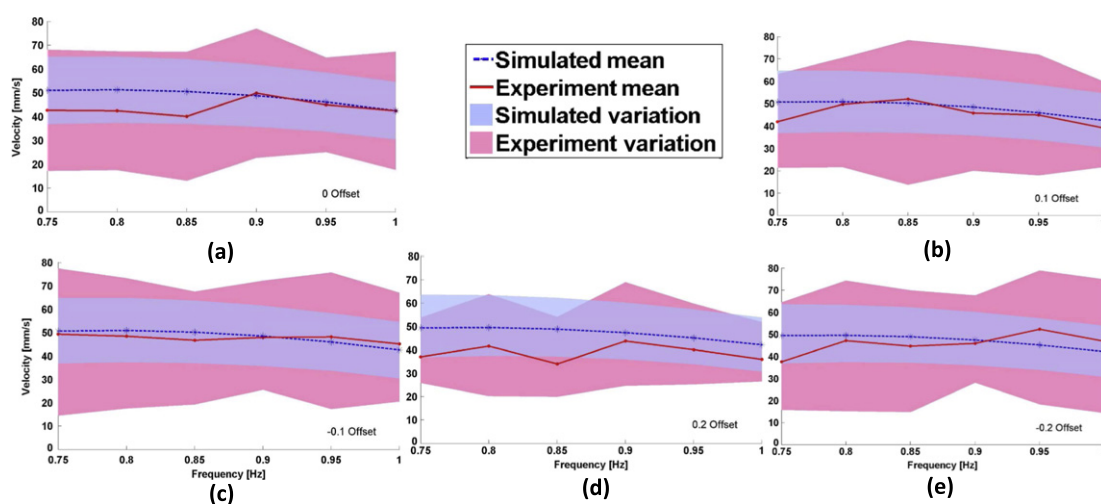

Figure 9. The center of mass (CoM) linear velocity and its standard deviation with respect to undulation frequency from 0.75–1 Hz for offset values of 0 (**a**), 0.1 (**b**), −0, 1 (**c**), 0.2 (**d**), and −0.2 (**e**). The red solid line and area represent experimental results, and the blue dashed line and area represent simulation results.
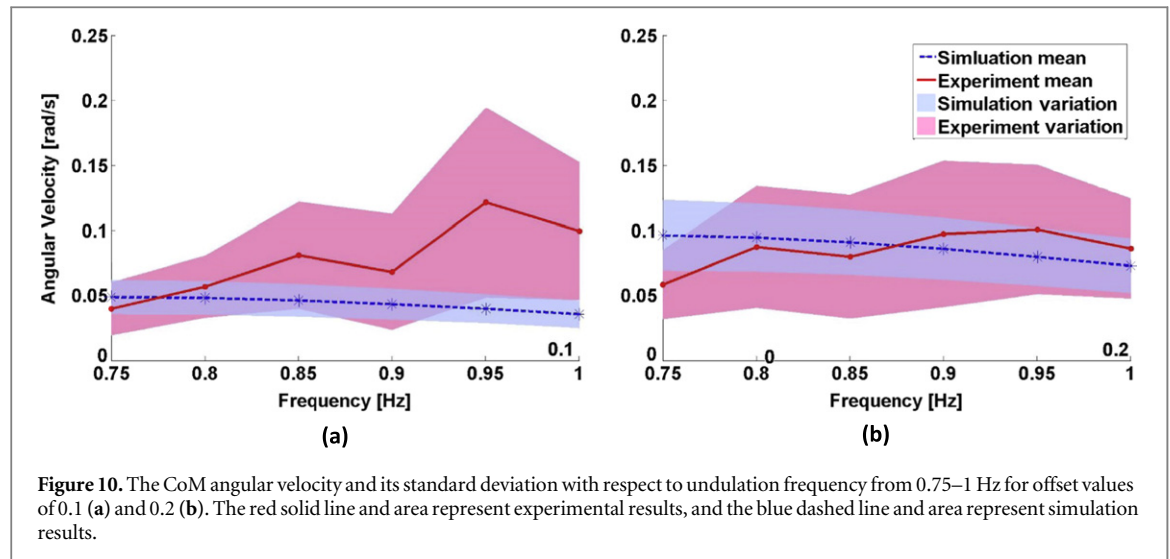
Figure 10. The CoM angular velocity and its standard deviation with respect to undulation frequency from 0.75–1 Hz for offset values of 0.1 (**a**) and 0.2 (**b**). The red solid line and area represent experimental results, and the blue dashed line and area represent simulation results.
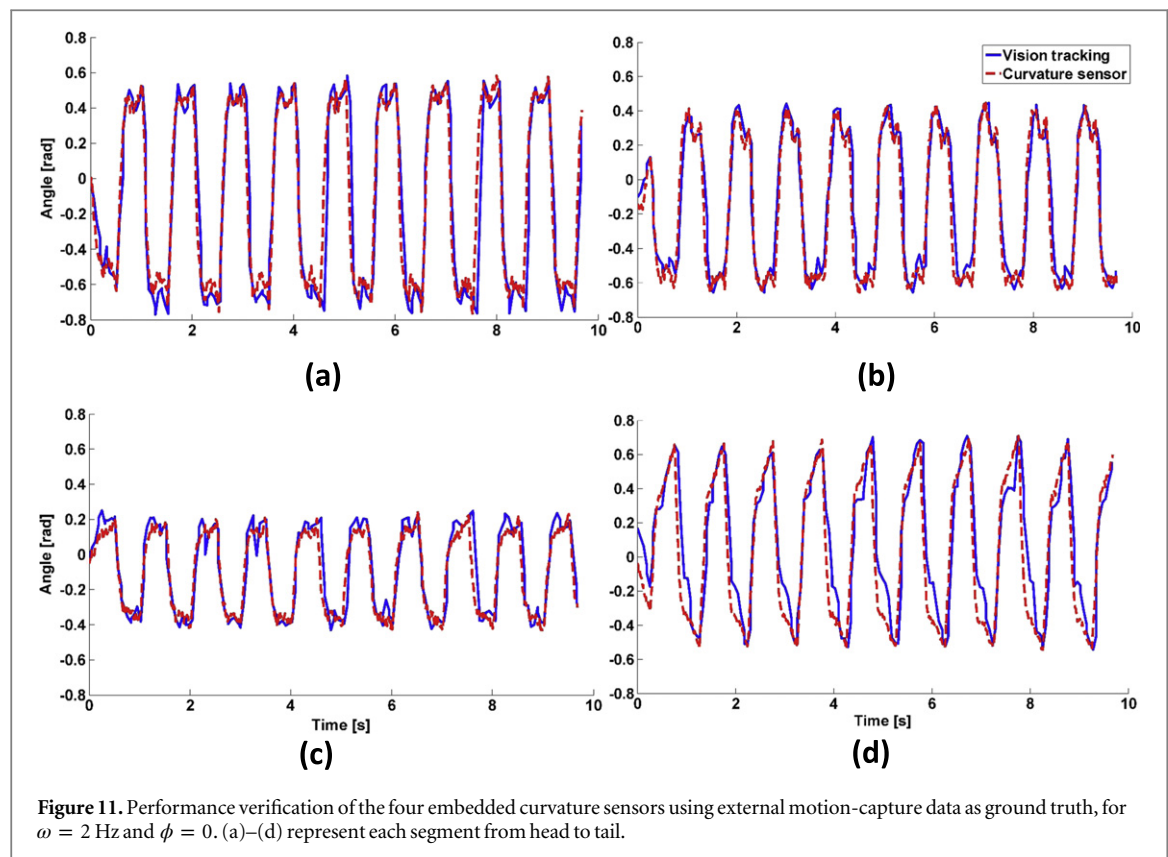
In order to verify the performance of the integrated curvature sensors, we first performed a line fit to the bending angle with respect to the sensor voltage data on preliminary characterization experiments. We then used this relation to compare curvatures recorded by the curvature sensors and external motion-capture system, which can be seen in figure 11. The curvature sensors measure the changing actuator angles with high sensitivity and low noise. No difference in quality is observed between the embedded and external measurement systems. Even though valves operate in binary open and close modes, this figure also displays the dynamic response of the actuators smoothing the square waveform to approximate a sinusoidal signal, which we consider as a form of physical intelligence, reducing low-level control requirements [16]. It can be seen that the first actuator (head) has the largest amplitude, and the third segment has the smallest amplitude. This is partially the result of differing inertias of the snake on either side of each actuator. For example, the first actuator has nothing in front of it to move, so it is free to curve with less constraint. This does not explain why the fourth actuator has a larger amplitude than the third, as the tail of the snake is where most of the mass is located and should be the most difficult to move. This behavior may be the result of fabrication and assembly errors, both of the soft core itself, and of the valve mounts. There may have been differences in the distances between the valve mounts, with the two mounts surrounding the third actuator being closer together, resulting in reduced curvature from that actuator and more from the surrounding ones. Finally, we observed that the front wheels of the tail assembly lift off the ground during locomotion, greatly reducing the lateral forces on the end of the fourth segment, allowing for greater bending deformation. A supplementary video is uploaded to demonstrate the locomotion of the SRS, also shown in figure 7.

4. Conclusion and future work

This article introduced the new generation of the WPI Soft Robotic Snake that achieves tether-free operation. This latest iteration was a step towards full autonomy, with an on-board microcontroller, pressure source, and distributed valving. In addition, it contains curvature sensors, which can sense the angle of each actuator segment precisely without the need for an external motion-capture system. We also developed a complete dynamic model of the SRS to take into account the full balance of forces and torques, allowing it to predict angular velocities. We demonstrated the accuracy of this model by comparing its results to the actual behavior of the SRS, with the discrepancies being a result of fabrication inconsistencies.

In order to reach the goal of full autonomy, additional work needs to be done on various aspects. First, the robot needs to be modified to allow for easier modifications and greater reliability. In this version of the SRS, it is really difficult to replace or modify a curvature sensor, as each sensor is embedded within the entire soft body of the snake, and replacing a single one requires replacing the body (or the equivalent of surgery). The same is true for a damaged actuator or threading. In order to solve this problem, future work aims to develop a snake robot with independent segments, which can be installed and replaced individually. This will allow for ease of experimentation and repair, letting the SRS function for extended testing scenarios.

Second, we plan to implement a high-level feedback control system for the SRS such that each segment performs corrections to its response to achieve desired linear and angular velocities. Motion planning based on this control system will take advantage of the benefits of its soft nature. Unlike for a rigid robot, the planning algorithm for our robot does not have to tightly constrain the task space. For instance, the SRS could move forward by utilizing contact forces from

Figure 11. Performance verification of the four embedded curvature sensors using external motion-capture data as ground truth, for $\omega = 2$ Hz and $\phi = 0$. (a)–(d) represent each segment from head to tail.

obstacles or wrap around objects to grasp them. Therefore, future work will study the detection and measurement of contact forces and positions to enable these capabilities.

References

[1] Trimmer B A, Takesian A E, Sweet B M, Rogers C B, Hake D C and Rogers D J 2006 *7th Int. Symp. on Technology and the Mine Problem* (Citeseer) 1 1–10

[2] Shepherd R F, Ilievski F, Choi W, Morin S A, Stokes A A, Mazzeo A D, Chen X, Wang M and Whitesides G M 2011 *Proc. Natl. Acad. Sci.* **108** 20400–3

[3] Skorina E H, Luo M, Ozel S, Chen F, Tao W and Onal C D 2015 *2015 IEEE Int. Conf. on Robotics and Automation (ICRA)* (Piscataway, NJ: IEEE)

[4] Luo M, Skorina E H, Tao W, Chen F and Onal C D 2015 *Proc. IEEE Int. Conf. on Technologies for Practical Robot Applications*

[5] Ranzani T, Cianchetti M, Gerboni G, de Falco I, Petroni G and Menciassi A 2013 *3rd Joint Workshop on New Technologies for Computer/Robot Assisted Surgery*

[6] Marchese A D, Katzschmann R K and Rus D 2014 *2014 IEEE/RSJ International Conference on Intelligent Robots and Systems (IROS 2014)* (Piscataway, NJ: IEEE) pp 554–60

[7] Morin S A, Shepherd R F, Kwok S W, Stokes A A, Nemiroski A and Whitesides G M 2012 *Science* **337** 828–32

[8] Cianchetti M, Licofonte A, Follador M, Rogai F and Laschi C 2014 *Actuators* vol 3 (Basel: MDPI) pp 226–44

[9] Laschi C and Cianchetti M 2014 *Frontiers Bioeng. Biotechnol.* **2** 3

[10] Kim S, Laschi C and Trimmer B 2013 *Trends Biotechnol.* **31** 287–94

[11] Majidi C 2014 *Soft Robotics* **1** 5–11

[12] Deimel R and Brock O 2014 *Robotics: Science and Systems* (Berkeley: CA) 1687–92 (www.roboticsproceedings.org/rss10/p18.pdf)

[13] Wakimoto S, Ogura K, Suzumori K and Nishioka Y 2009 *Robotics and Automation, 2009. ICRA'09 IEEE Int. Conf. on Robotics and Automation (ICRA'09)* (Piscataway, NJ: IEEE) pp 556–61

[14] Onal C D, Chen X, Whitesides G M and Rus D 2011 *Int. Symp. on Robotics Research (ISRR)*

[15] Marchese A D, Onal C D and Rus D 2012 *Int. Symp. on Experimental Robotics*

[16] Onal C D and Rus D 2013 *Bioinspiration Biomimetics* **8** 026003

[17] Marchese A D, Onal C D and Rus D 2014 *Soft Robotics* **1** 75–87

[18] Marchese A D, Onal C D and Rus D 2013 *Springer Tracts in Advanced Robotics (STAR)* vol 88 (Berlin: Springer) pp 41–54

[19] Tolley M T, Shepherd R F, Mosadegh B, Galloway K C, Wehner M, Karpelson M, Wood R J and Whitesides G M 2014 *Soft Robotics* **1** 213–23

[20] Tolley M T, Shepherd R F, Karpelson M, Bartlett N W, Galloway K C, Wehner M, Nunes R, Whitesides G M and Wood R J 2014 *IEEE/RSJ Int. Conf. on Intelligent Robots and Systems* pp 561–6

[21] Wehner M, Tolley M T, Mengüç Y, Park Y L, Mozeika A, Ding Y, Onal C D, Shepherd R F, Whitesides G M and Wood R J 2014 *Soft Robotics* **1** 263–74

[22] Luo M, Agheli M and Onal C D 2014 *Soft Robotics* **1** 136–46

[23] Luo M, Agheli M and Onal C D 2014 *ASME 2014 Int. Design Engineering Technical Conferences and Computers and Information in Engineering Conf.* (American Society of Mechanical Engineers) p V05BT08A102

[24] Hirose S 1993 *Biologically Inspired Robots: Snake-like Locomotors and Manipulators* (Oxford: Oxford University Press)

[25] McKenna J C, Anhalt D J, Bronson F M, Brown H B, Schwerin M, Shammas E and Choset H 2008 *IEEE Int. Conf. on Robotics and Automation (ICRA 2008)* pp 1150–55

[26] Wright C, Buchan A, Brown B, Geist J, Schwerin M, Rollinson D, Tesch M and Choset H 2012 *IEEE Int. Conf. on Robotics and Automation (ICRA)* pp 4347–54

[27] Transeth A A, Leine R I, Glocker C, Pettersen K Y and
     Liljeback P 2008 *IEEE Trans. on Robotics* **24** 88–104
[28] Crespi A and Ijspeert A J 2008 *IEEE Trans. on Robotics* **24** 75–87
[29] Luo M, Tao W, Chen F, Khuu T K, Ozel S and Onal C D 2014
     *Proc. IEEE Int. Conf. on Technologies for Practical Robot
     Applications*
[30] Luo M, Pan Y, Tao W, Chen F, Skorina E H and Onal C D 2015
     *ASME 2015 Int. Design Engineering Technical Conf. (American
     Society of Mechanical Engineers)*
[31] Cianchetti M, Renda F, Licofonte A and Laschi C 2012 *4th
     IEEE RAS & EMBS Int. Conf. on Biomedical Robotics and
     Biomechatronics (BioRob)* (Piscataway, NJ: IEEE) pp 634–39
[32] Webster R J and Jones B A 2010 *Int. J. Robot. Res.* **29** 1661–83
[33] Pettersen K Y, Stavdahl Ø and Gravdahl J T 2013 *Snake Robots:
     Modelling, Mechatronics, and Control* (Berlin: Springer)
[34] Sato M, Fukaya M and Iwasaki T 2002 *Control Syst.* 22
     (Piscataway, NJ: IEEE) pp 64–81
[35] Ma S 2001 *Adv. Robot.* **15** 205–24
[36] Transeth A A, Pettersen K Y and Liljebäck P 2009 *Robotica* **27** 999–1015
[37] Hoshi Y *et al* 2001 *American Control Conference* vol 1
     (Piscataway, NJ: IEEE) 113–18
[38] Bayraktaroglu Z 2009 *Mech. Mach. Theory* **44** 591–602
[39] Rollinson D, Alwala K V, Zevallos N and Choset H 2014 *IEEE/
     RSJ Int. Conf. on Intelligent Robots and Systems (IROS 2014)*
     (Piscataway, NJ: IEEE) 1093–99
[40] Kano T, Sato T, Kobayashi R and Ishiguro A 2012
     Bioinspiration Biomimetics **7** 046008
[41] Ozel S, Keskin N A, Khea D and Onal C D 2015 *Sensors and
     Actuators A* submitted